Chapter 14
Constrained Reconstructions in X-ray Phase Contrast Imaging: Uniqueness, Stability and Algorithms

Simon Maretzke and Thorsten Hohage

Abstract This chapter considers the inverse problem of X-ray phase contrast imaging (XPCI), as introduced in Chap. 2. It is analyzed how physical a priori knowledge, e.g. of the approximate size of the imaged sample (support knowledge), affects the inverse problem: uniqueness and—for a linearized model—even well-posedness are shown to hold under support constraints, ensuring stability of reconstruction from real-world noisy data. In order to exploit these theoretical insights, regularized Newton methods are proposed as a class of reconstruction algorithms that flexibly incorporate constraints and account for the inherent nonlinearity of XPCI. A Kaczmarz-type variant of the approach is considered for 3D image-recovery in tomographic XPCI, which remains applicable for large-scale data. The relevance of constraints and the capabilities of the proposed algorithms are demonstrated by numerical reconstruction examples.

2010 Mathematics Subject Classification: 65R10 · 65R32 · 78A45 · 78A46 · 92C55 · 94A08

14.1 Forward Models

We aim to describe (propagation-based) X-ray phase contrast imaging (XPCI) in the language of inverse problems. To this end, we deduce *forward operators* $F : X \to Y$, that model the dependence of the measured near-field diffraction patterns (called *holograms*) $I \in Y$ from the sample-characterizing parameters $f \in X$ (the sought *image*). Different models F are obtained for various settings of practical interest, including X-ray phase contrast tomography (XPCT).

S. Maretzke (✉) · T. Hohage
Institute for Numerical and Applied Mathematics, Universität Göttingen, Lotzestr. 16-18, 37083 Göttingen, Germany
e-mail: s.maretzke@math.uni-goettingen.de

T. Hohage
e-mail: hohage@math.uni-goettingen.de

T. Salditt et al. (eds.), *Nanoscale Photonic Imaging*, Topics in Applied Physics 134,
https://doi.org/10.1007/978-3-030-34413-9_14

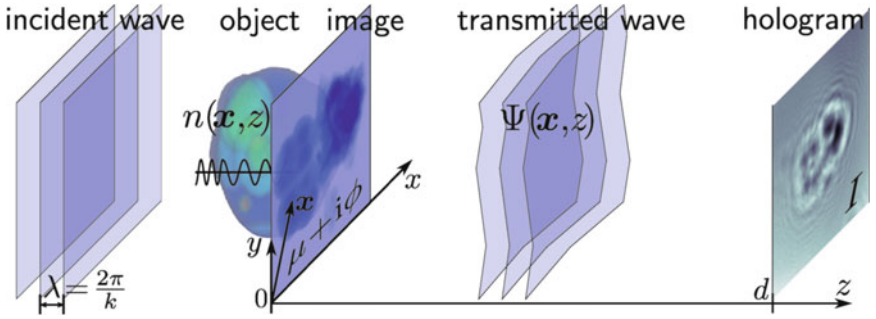

Fig. 14.1 Basic physical model of XPCI: incident plane waves scatter on the imaged object, that is parametrized by a spatially varying refractive index n. The resulting diffraction-pattern (hologram) is recorded in the optical near-field at some distance behind the sample

14.1.1 Physical Model and Preliminaries

The basic physical model of XPCI is detailed in Chap. 2 and summarized by Fig. 14.1: incident monochromatic X-rays, modeled by plane waves, are scattered by the imaged sample, that is parametrized by its spatially varying refractive index $n(\boldsymbol{x}, z) = 1 - \delta(\boldsymbol{x}, z) + \mathrm{i}\beta(\boldsymbol{x}, z)$ (δ, β: refractive- and absorption decrement). By the scattering-interaction, a perturbation (the image) is imprinted upon the transmitted X-ray wave-field. The intensity I of the perturbed wave-field is recorded by a detector placed at a finite distance $d > 0$ behind the sample.

As derived in Sect. 2.1, the dependence of the hologram-intensities I from the sample-parameters δ and β is given by

$$I(\boldsymbol{x}) = |\Psi(\boldsymbol{x}, d)|^2 = |\mathcal{D}(\exp(-\mu - \mathrm{i}\phi))(\boldsymbol{x})|^2 \qquad \text{for all} \qquad \boldsymbol{x} \in \mathbb{R}^2,$$
$$\phi(\boldsymbol{x}) = k \int_{\mathbb{R}} \delta(\boldsymbol{x}, z)\, \mathrm{d}z, \qquad \mu(\boldsymbol{x}) := k \int_{\mathbb{R}} \beta(\boldsymbol{x}, z)\, \mathrm{d}z. \tag{14.1}$$

The *phase-* and *absorption-images* ϕ and μ are 2D-*projections* of the 3D-densities δ and β (k: X-ray wavenumber) along the incident z-direction. The *Fresnel-propagator* $\mathcal{D}$, modeling free-space propagation of the X-rays between object and detector, is defined by

$$\mathcal{D}(f) \mapsto \mathcal{F}\left(m_{\mathfrak{f}} \cdot \mathcal{F}^{-1}(f)\right) \qquad \text{with} \qquad m_{\mathfrak{f}}(\boldsymbol{\xi}) := \exp\left(-\mathrm{i}\boldsymbol{\xi}^2/(2\mathfrak{f})\right). \tag{14.2}$$

Here, $\mathcal{F}(f)(\boldsymbol{\xi}) := (2\pi)^{-m/2} \int_{\mathbb{R}^m} \exp(-\mathrm{i}\boldsymbol{\xi} \cdot \boldsymbol{x}) f(\boldsymbol{x})\, \mathrm{d}\boldsymbol{x}$ is the Fourier-transform and $\mathfrak{f} = kb^2/d > 0$ is the modified[1] Fresnel-number associated with the physical length b, that is identified with 1 in the chosen dimensionless coordinates.

[1] The classical Fresnel-number is given by $\mathfrak{f}_{(b)} := b^2/(\lambda d) = \mathfrak{f}/(2\pi)$. However, using the parameter $\mathfrak{f}$ is notationally more convenient as it avoids excessive occurence of 2π-factors.

XPCI-experiments provide intensity data I of the form (14.1) (up to data errors), whereas the images ϕ, μ are the quantities of interest. Hence, the following principal *inverse problem* has to be solved:

Inverse Problem 1 (XPCI) *For some set A, reconstruct a 2D-image* $h = \mu + i\phi \in A$ *from measured holograms I of the form (14.1).*

By rotating the object in Fig. 14.1, holograms $I_{\boldsymbol{\theta}_j}$ may be acquired for different *incident directions* $\boldsymbol{\theta}_j \in \mathbb{S}^2 = \{\boldsymbol{x} \in \mathbb{R}^3 : |\boldsymbol{x}| = 1\}$ of the X-rays onto the sample (in Fig. 14.1, the incident direction coincides with the z-axis). This is the setting of X-ray phase contrast *tomography* (XPCT). A mathematical model will be provided in Sect. 14.1.3. XPCT allows to probe *3D*-variations of the parameters δ, β beyond mere projections ϕ, μ.

Inverse Problem 2 (XPCT) *For some set A, recover a* 3D*-image* $f = k\beta + ik\delta \in A$ *from holograms* $\{I_{\boldsymbol{\theta}_j}\}$ *measured under different incident directions* $\{\boldsymbol{\theta}_j\} \subset \mathbb{S}^2$.

14.1.1.1 A Priori Constraints

The set of admissible images A in inverse Problems 1 and 2 is highly relevant. In order to facilitate and stabilize image reconstruction, the set A should be restricted as far as possible by available physical a priori knowledge:

- *Support constraints*: real-world samples are of finite size. This implies that the functions $f \in \{\phi, \mu, \delta, \beta\} : \mathbb{R}^m \to \mathbb{R}$ have a *compact support*, i.e. are identically zero outside some bounded *object-domain* $\Omega \subset \mathbb{R}^m$.
- *Non-negativity*: by the physics of hard X-rays, the decrements δ, β—and thus also ϕ, μ—are always non-negative.
- *Pure phase object*: especially for biological samples, β and μ are typically orders of magnitude smaller than δ and ϕ. Assuming a purely shifting-, i.e. *non-absorbing* object β, $\mu = 0$, is then a good approximation.
- *Homogeneous objects*: as is rigorously true for samples composed of a single material, proportionality of δ and β [ϕ and μ] may often be assumed.
- *Regularity*: realistic images ϕ, μ, δ, β are not arbitrarily singular functions, but typically have some characteristic smoothness properties.
- *Tomographic consistency*: Images ϕ and μ that arise as tomographic projections of one object under different incident directions are correlated.

Focussing on support-knowledge, we study the role of such *constraints* on inverse Problems 1 and 2 and outline how to exploit them algorithmically.

14.1.1.2 Additional Notation

We study inverse Problems 1 and 2 in spaces of square-integrable functions:

$$L^2(\mathbb{R}^m) = \{f : \mathbb{R}^m \to \mathbb{C} : \|f\|_{L^2} < \infty\}, \quad \|f\|_{L^2}^2 := \int_{\mathbb{R}^m} |f(\boldsymbol{x})|^2 \, \mathrm{d}\boldsymbol{x} \tag{14.3}$$

The focus lies on functions $f \in L^2(\mathbb{R}^m)$ that have *compact support* $\mathrm{supp}(f)$, i.e. that vanish outside some bounded domain $\Omega \subset \mathbb{R}^m$:

$$\mathrm{supp}(f) \subset \Omega \;:\Leftrightarrow\; f|_{\mathbb{R}^m \setminus \Omega} = 0, \tag{14.4}$$

$f|_B$ denotes the *restriction* of f to $B \subset \mathbb{R}^m$, defined by $f|_B(\boldsymbol{x}) = f(\boldsymbol{x})$ if $\boldsymbol{x} \in B$ and $f|_B(\boldsymbol{x}) = 0$ otherwise. For $\Omega \subset \mathbb{R}^m$, we write

$$L^2(\Omega) = \{f \in L^2(\mathbb{R}^m) : \mathrm{supp}(f) \subset \Omega\}. \tag{14.5}$$

Furthermore, we define spaces of *real-valued* L^2-functions:

$$L^2(\Omega, \mathbb{R}) = \{f \in L^2(\Omega) : \mathrm{Im}(f) = 0\}, \tag{14.6}$$

where $\mathrm{Re}(\cdot)$, $\mathrm{Im}(\cdot)$ denote the real- and imaginary parts, respectively.

14.1.2 Forward Operators for XPCI

Based on Sect. 14.1.1, we introduce forward maps $F : X \to Y$ modeling different settings of XPCI. Note that we define the maps in arbitrary dimensions $m \in \{1, 2, 3, \ldots\}$ although the natural case are images and holograms in $m = 2$ dimensions. The benefit of this will be seen in Sect. 14.3.4.1.

14.1.2.1 General Nonlinear Forward Operator

The most general (and most challenging) XPCI-setting is the reconstruction of both phase ϕ and absorption μ from a single hologram. According to (14.1), this setting is modeled by the forward map

$$\mathcal{N}(h) = I - 1 = |\mathcal{D}(\exp(-h))|^2 - 1, \tag{14.7}$$

for *complex-valued* images $h = \mu + \mathrm{i}\phi$. Note that the constant background intensity 1 has been subtracted, such that $\mathcal{N}(0) = 0$. As a benefit, $\mathcal{N}$ can be analyzed as an operator on L^2-spaces: for any bounded $\Omega \subset \mathbb{R}^m$,

$$\mathcal{N} : L^2(\Omega) \to L^2(\mathbb{R}^m) \tag{14.8}$$

is essentially[2] a well-defined, *nonlinear* operator. Moreover, it can be shown [1, 2] that $\mathcal{N}$ is continuously Fréchet-differentiable, i.e. sufficiently smooth to admit local linear approximations. The derivative is given by

$$\mathcal{N}'[f]h = -2\mathrm{Re}\big(\overline{\mathcal{D}\left(\exp\left(-f\right)\right)} \cdot \mathcal{D}\left(\exp\left(-f\right) \cdot h\right)\big). \tag{14.9}$$

14.1.2.2 Linearized Forward Map and Contrast-Transfer-Functions

The nonlinearity of the forward map $\mathcal{N}$ causes difficulties in both analysis and practical image reconstruction. It is therefore standard [3–7] to resort to a *linearization* valid for weakly scattering samples (see e.g. [7] for details on the regime-of-validity): the idea is that the image f is sufficiently "small" so that higher-order terms are negligible:

$$\mathcal{N}(h) = \mathcal{T}(h) + \mathcal{O}(h^2) \approx \mathcal{T}(h) \quad \text{with} \quad \mathcal{T}(h) := -2\mathrm{Re}\left(\mathcal{D}(h)\right). \tag{14.10}$$

The linearized forward map $\mathcal{T} = \mathcal{N}'[0]$ is also known as the *contrast-transfer-function-* (CTF-)model, which refers to the following alternate form (compare with Sect. 2.2):

$$\mathcal{T}(-\mu - \mathrm{i}\phi) = -2\mathcal{F}^{-1}\Bigg(\underbrace{\sin\left(\frac{|\boldsymbol{\xi}|^2}{2\mathfrak{f}}\right)}_{=:s_0(\boldsymbol{\xi})}\mathcal{F}(\phi) + \underbrace{\cos\left(\frac{|\boldsymbol{\xi}|^2}{2\mathfrak{f}}\right)}_{=:c_0(\boldsymbol{\xi})}\mathcal{F}(\mu)\Bigg) \tag{14.11}$$

According to (14.11), the linearized contrast in Fourier-space is given by a superposition of the Fourier-transforms of phase- and absorption-image ϕ, μ modulated by the oscillatory CTFs s_0 and c_0, respectively.

As $|s_0(\boldsymbol{\xi})|, |c_0(\boldsymbol{\xi})| \leq 1$ for all $\boldsymbol{\xi} \in \mathbb{R}^m$, $\mathcal{T} : L^2(\mathbb{R}^m) \to L^2(\mathbb{R}^m)$ is a bounded $(\mathbb{R})$-linear operator with $\|\mathcal{T}(h)\|_{L^2} \leq 2\|h\|_{L^2}$ for all $h \in L^2(\mathbb{R}^m)$.

14.1.2.3 Homogeneous Objects and Pure Phase Objects

The cases of *homogeneous objects* and *pure phase objects*, see Sect. 14.1.1.1, may be treated in a unified manner, by expressing the complex-valued image $h = \mu + \mathrm{i}\phi = \mathrm{i}\mathrm{e}^{-\mathrm{i}\nu}\varphi$ in terms of a single *real-valued* function φ and a parameter $\nu = \arctan(\beta/\delta) \in [0; \pi/2)$ ($\nu = 0$: pure phase object).

Such a *homogeneity-constraint* may be incorporated into the general forward model, via a modified forward map

[2] To ensure well-definedness on the whole space $L^2(\Omega)$, the exponential has to be suitably truncated for the physically irrelevant case of negative absorption $\mathrm{Re}(f) = \mu < 0$.

$$\mathscr{N}_\nu : L^2(\Omega, \mathbb{R}) \to L^2(\mathbb{R}^m);$$
$$\varphi \mapsto \mathscr{N}(\mathrm{i}e^{-\mathrm{i}\nu}\varphi) = \left|\mathcal{D}\left(\exp(-\mathrm{i}e^{-\mathrm{i}\nu}\varphi)\right)\right|^2 - 1. \tag{14.12}$$

The linearized model under a homogeneity constraint may be expressed via a single CTF $s_\nu(\boldsymbol{\xi}) := \sin\left(|\boldsymbol{\xi}|^2/(2\mathfrak{f}) + \nu\right)$: for $\varphi \in L^2(\mathbb{R}^m, \mathbb{R})$, it holds that

$$\mathscr{S}_\nu(\varphi) := -2\mathcal{F}^{-1}\left(s_\nu \cdot \mathcal{F}(\varphi)\right) = \mathscr{T}(\mathrm{i}e^{-\mathrm{i}\nu}\varphi). \tag{14.13}$$

Although (14.13) only holds for real-valued φ, we define $\mathscr{S}_\nu : L^2(\mathbb{R}^m) \to L^2(\mathbb{R}^m)$ ($\|\mathscr{S}_\nu\| = 2$) on general L^2-spaces. For its properties, it is widely irrelevant if real- or complex-valued functions are considered, as $\mathscr{S}_\nu$ commutes with the pointwise real-part: $\mathrm{Re}\,(\mathscr{S}_\nu(h)) = \mathscr{S}_\nu(\mathrm{Re}\,(h))$ for all $h \in L^2(\mathbb{R}^m)$.

14.1.2.4 Multiple Holograms

In order to obtain richer data in XPCI, it is standard to acquire multiple holograms $I_1, I_2, \ldots, I_\ell$ at several object-to-detector-distances, corresponding to different Fresnel-numbers $\mathfrak{f}_1, \mathfrak{f}_2, \ldots, \mathfrak{f}_\ell$. This may be modeled by combining the forward maps for the individual holograms $F_j : X \to L^2(\mathbb{R}^m)$; $h \mapsto I_j - 1$, $F_j \in \{\mathscr{N}^{(\mathfrak{f}_j)}, \mathscr{N}_\nu^{(\mathfrak{f}_j)}, \mathscr{T}^{(\mathfrak{f}_j)}, \mathscr{S}_\nu^{(\mathfrak{f}_j)}\}$ to a "vector-valued" operator:

$$F^{(\mathfrak{f}_1,\ldots,\mathfrak{f}_\ell)} : X \to L^2(\mathbb{R}^m)^\ell;\ h \mapsto (F_1(h), \ldots, F_\ell(h)) \tag{14.14}$$

14.1.3 Forward Operators for XPCT

In X-ray phase contrast tomography (XPCT), holograms are measured under different incident directions $\boldsymbol{\theta} \in \mathbb{S}^2$. According to the basic model (14.1), the resulting intensities $I_{\boldsymbol{\theta}}$ are then given by

$$I_{\boldsymbol{\theta}} = \left|\mathcal{D}\left(\exp\left(-\mathscr{P}_{\boldsymbol{\theta}}(k\beta + \mathrm{i}k\delta)\right)\right)(\boldsymbol{x})\right|^2, \tag{14.15}$$

where $\mathscr{P}_{\boldsymbol{\theta}}$ is the parallel-beam projector along $\boldsymbol{\theta}$ ($\boldsymbol{\theta} \perp \boldsymbol{n}_x \perp \boldsymbol{n}_y \perp \boldsymbol{\theta}$):

$$\mathscr{P}_{\boldsymbol{\theta}}(f)(x, y) := \int_{\mathbb{R}} f(x\boldsymbol{n}_x + y\boldsymbol{n}_y + z\boldsymbol{\theta})\,\mathrm{d}z, \quad x, y \in \mathbb{R}, \tag{14.16}$$

According to the standard theory of computed tomography, projection-data $\{\mathscr{P}_{\boldsymbol{\theta}}(f)\}_{\boldsymbol{\theta}\in\Theta}$ for a suitable set of incident-directions Θ allows to reconstruct the underlying 3D-function $f : \mathbb{R}^3 \to \mathbb{C}$. Analogously, the goal of XPCT is to reconstruct 3D-variations of the decrements δ and β of the sample's refractive index from a tomographic series of holograms $\{I_{\boldsymbol{\theta}}\}_{\boldsymbol{\theta}\in\Theta}$.

Composition of the projectors $\mathscr{P}_{\boldsymbol{\theta}}$ with any of the forward maps $F \in \{\mathscr{N}, \mathscr{N}_\nu, \mathscr{T}, \mathscr{S}_\nu\} : X \to L^2(\mathbb{R}^m)$ from Sect. 14.1.2 induces a corresponding XPCT-model: for $\Theta = \{\boldsymbol{\theta}_1, \ldots, \boldsymbol{\theta}_t\}$, the tomographic hologram-data is modeled by

$$F_{\mathrm{PCT}} : f \mapsto \left(F\left(\mathscr{P}_{\boldsymbol{\theta}}(f)\right)\right)_{\boldsymbol{\theta}\in\Theta} = \left(I_{\boldsymbol{\theta}} - 1\right)_{\boldsymbol{\theta}\in\Theta}. \tag{14.17}$$

14.2 Uniqueness Theory

In practice, it is highly relevant whether the measured intensity data I uniquely determines the sought image $h = \mu + \mathrm{i}\phi$ (or $f = k\beta + \mathrm{i}k\delta$ in XPCT). Otherwise, it might happen that two structurally different samples are indistinguishable by the imaging method, which is not desirable. (Non-)uniqueness of an inverse problem is equivalent to (non-)injectivity of the governing forward operator $F : X \to Y$. Hence, it depends on different aspects:

1. The richness of the data, i.e. the size of the *data-space* Y: for example, it is commonly argued that measuring several holograms $I_1, I_2, \ldots$ at different Fresnel-numbers (see Sect. 14.1.2.4) helps to ensure uniqueness in XPCI.
2. Available a priori knowledge, i.e. the size of the *object-space* X: the smaller X the more likely it is that any two images $h_1, h_2 \in X$ with $h_1 \neq h_2$ induce distinguishable data $F(h_1) \neq F(h_2)$.

In addition, it may happen that the nonlinear forward model is unique but its linearization is non-unique or vice verser. Accordingly, the different forward models from Sect. 14.1.2 have to be investigated individually.

14.2.1 Preliminary Results and Counter-Examples

We first review some known results on (non-)uniqueness of XPCI. Firstly, image reconstruction from a single hologram is generally *non-unique*:

- Linearized model: $\mathscr{T} : L^2(\mathbb{R}^m) \to L^2(\mathbb{R}^m);\ h \mapsto -2\mathrm{Re}(h)$ has a huge null-space composed of all h for which $\mathcal{D}(h)$ is purely imaginary-valued:

$$\ker(\mathscr{T}) := \{h \in L^2(\mathbb{R}^m) : \mathscr{T}(h) = 0\} = \mathcal{D}^{-1}\left(\mathrm{i}L^2(\mathbb{R}^m, \mathbb{R})\right) \tag{14.18}$$

- Nonlinear model (example from [8]): Images $h_\pm : \mathbb{R}^2 \setminus \{0\} \to \mathbb{C};\ \boldsymbol{x} \mapsto a(|\boldsymbol{x}|) \pm \mathrm{i}\nu \arctan2(\boldsymbol{x})$ for $\nu \in \mathbb{N}$ and smooth functions $a : \mathbb{R}_{\geq 0} \to \mathbb{R}$ give rise to so-called *phase-vortices* in the wave-field. The sign of the vortex is not determined by Fresnel-intensities ($A := \exp(-a)$):

$$|\mathcal{D}(\exp(-h_+))|^2 = |\mathcal{D}(A \cdot \exp(-\mathrm{i}\nu \arctan2(\cdot))|^2$$
$$= |\mathcal{D}(A \cdot \exp(\mathrm{i}\nu \arctan2(\cdot))|^2 = |\mathcal{D}(\exp(-h_-))|^2 \quad (14.19)$$

Based on these negative results, it is typically argued that at least two holograms and/or a homogeneity-constraint are required for uniqueness. Indeed, the situation improves substantially in the latter settings:

- Uniqueness under homogeneity-constraints (linear): the operator $\mathscr{S}_\nu : L^2(\mathbb{R}^m) \to L^2(\mathbb{R}^m)$ from Sect. 14.1.2.3 is *injective*, as the zero-manifolds of the Fourier-multiplier s_ν are sets of the Lebesgue-measure 0 in $\mathbb{R}^m$.
- Uniqueness for two holograms (linear): in [9], it is shown by a similar argument based on the CTF-representation (14.11) that also the operator $\mathscr{T}^{(\mathfrak{f}_1,\mathfrak{f}_2)} : L^2(\mathbb{R}^m) \to L^2(\mathbb{R}^m)^2$ (see Sect. 14.1.2.4) is injective for $\mathfrak{f}_1 \neq \mathfrak{f}_2$.

Moreover, it is argued in [9] that both results carry over to the nonlinear model, provided that the image h is *compactly supported*. Indeed, a much stronger uniqueness result holds true under such an assumption, as will be seen in the following.

14.2.2 Sources of Non-uniqueness—The Phase Problem

According to the basic physical model (14.1), image-formation mathematically amounts to three operations: pointwise exponential, $h \mapsto \exp(-h)$, Fresnel-propagation, $\exp(-h) \mapsto \mathcal{D}(\exp(-h))$, and computation of the pointwise squared modulus, $\mathcal{D}(\exp(-h)) \mapsto |\mathcal{D}(\exp(-h))|^2$. Among those, $\mathcal{D}$ is an *invertible* operation, i.e. does not destroy information. This is not true for the other two operations, which give rise to different sources of non-uniqueness:

- *Phase-wrapping*: The exponential is 2π-periodic in the imaginary-part of its argument. Hence, the *phase-image* $\phi = \mathrm{Im}(h)$ may only be determined by the data up to increments by multiples of 2π.
- *Phase problem*: The squared modulus, arising from the restriction of X-ray detectors to measuring *intensities*, eliminates the phase-information.

The first aspect is simpler to analyze and often turns out to be of lesser practical impact in XPCI: for moderately strongly scattering samples, ϕ is a priori known to assume values within $[0; 2\pi)$, so that non-uniqueness due to *phase-wrapping* is not an issue. In the following, we therefore focus on possible ambiguities due to the phase problem.

14.2.3 Relation to Classical Phase Retrieval Problems

Up to possibly remaining phase-wrapping ambiguities, the image reconstruction problem in XPCI may be rephrased as follows:

Given data $I = |\mathcal{D}(O)|^2$, reconstruct the object-transmission-function (OTF) $O := \exp(-h) \in \tilde{A}$ from some admissible set $\tilde{A}$.

Such settings are known as *phase retrieval* problems as recovering O is equivalent to retrieving the missing phase of $\mathcal{D}(O)$ (and then inverting $\mathcal{D}$). Uniqueness of phase retrieval has been extensively studied ever since the pioneering works of Walther [10] and Akutowicz [11, 12], primarily for the case where $\mathcal{D}$ is replaced by the Fourier-transform $\mathcal{F}$, i.e. for the reconstruction from phaseless Fourier-data. We refer to [13–17] for reviews.

Indeed, Fresnel-data may be readily reduced to the classical Fourier-setting, by rewriting the Fresnel-propagator in the form

$$\mathcal{D}(f)(\boldsymbol{x}) = u_0 \mathfrak{f}^{\frac{m}{2}} n_{\mathfrak{f}}(\boldsymbol{x}) \cdot \mathcal{F}\left(n_{\mathfrak{f}} \cdot f\right)(\mathfrak{f}\boldsymbol{x}) \qquad \text{for all} \qquad \boldsymbol{x} \in \mathbb{R}^m \tag{14.20}$$

with $n_{\mathfrak{f}}(\boldsymbol{x}) = \exp(\mathrm{i}\mathfrak{f}\boldsymbol{x}^2/2)$ and $u_0 = \exp(-\mathrm{i}m\pi/4)$. Hence, if we define $\tilde{O} := n_{\mathfrak{f}} \cdot O$, then the holograms in XPCI provide Fourier-data for $\tilde{O}$:

$$I(\boldsymbol{\xi}/\mathfrak{f}) = |\mathcal{D}(O)(\boldsymbol{\xi}/\mathfrak{f})|^2 = \mathfrak{f}^m \mathcal{F}(\tilde{O})(\boldsymbol{\xi}) \qquad \text{for all} \qquad \boldsymbol{\xi} \in \mathbb{R}^m. \tag{14.21}$$

Based on the identification in (14.21), uniqueness results for Fourier-phase retrieval may be adapted to the Fresnel-regime. Notably, however, most of such uniqueness theorems assume a compact support of the objective. Importantly, this is *not* justified in the setting of XPCI:

The OTF O is *not* a compactly supported function in any realistic setting. Only the *contrast* $o := O - 1$ typically has compact support.

14.2.4 Holographic Nature of Phase Retrieval in XPCI

In order to emphasize the structural difference to classical phase retrieval problems, it is illustrative to rewrite the XPCI-model in the form

$$I = |\mathcal{D}(O)|^2 = |\mathcal{D}(1) + \mathcal{D}(o)|^2 = 1 + \underbrace{2\mathrm{Re}(\mathcal{D}(o))}_{=\mathcal{D}(o)+\overline{\mathcal{D}(o)}} + |\mathcal{D}(o)|^2\,, \tag{14.22}$$

where it has been used that $\mathcal{D}$ maps constant functions onto themselves.[3] According to the physical model from Sect. 14.1.1, the summands on the r.h.s. of (14.22) can be interpreted in terms of the *scattered*- and *transmitted* parts of the X-ray wave-field: the constant 1 is the intensity of the incident plane wave and the last summand that of the waves scattered by the object, whereas the second term describes the *interference* of these two wave-field components on the detector.

Formula (14.22) places the inverse problem of XPCI in the realm of *holographic* phase retrieval problems, i.e. reconstruction in the presence of a *reference signal*—here provided by the unscattered part of the incident X-rays. Several theoretical and practical works have shown that such a holographic reference facilitates phase retrieval, see e.g. [18–21].

14.2.5 General Uniqueness Under Support Constraints

According to (14.22), image reconstruction in XPCI is equivalent to retrieving $o = \exp(-h) - 1$ from data of the form (14.22) (up to possible phase-wrapping). By invertibility of the Fresnel-propagator $\mathcal{D}$, uniqueness thus holds if it is possible to disentangle the summands $\mathcal{D}(o)$, $\overline{\mathcal{D}(o)}$, and $|\mathcal{D}(o)|^2$. As shown in [22] using the theory of entire functions, the latter is indeed possible whenever o is known to have compact support, which is true for any sample of finite size. The principal result reads as follows:

Theorem 14.1 (Uniqueness of XPCI [22]) *Let o (= $\exp(-h) - 1$) be a compactly supported function (or* distribution*).*

Then o is uniquely determined by XPCI-data $I = |\mathcal{D}(1 + o)|^2$. Furthermore, uniqueness is retained if only restricted *data $I|_K$ is available, measured for any* detection-domain *$K \subset \mathbb{R}^m$ that contains an open set.*

For any such K and $\Omega \subset \mathbb{R}^m$ bounded, $\mathcal{N}_K : h \mapsto \mathcal{N}(h)|_K$ is injective *up to phase-wrapping: if $\mathcal{N}(h_1)|_K = \mathcal{N}(h_2)|_K$ for $h_1, h_2 \in L^2(\Omega)$, then*

$$h_1(\boldsymbol{x}) - h_2(\boldsymbol{x}) \in 2\pi i\mathbb{Z} \quad \text{for almost all} \quad \boldsymbol{x} \in \mathbb{R}^m. \tag{14.23}$$

Importantly, Theorem 14.1 establishes uniqueness in the most challenging setting of XPCI: single hologram, no homogeneity-constraint. The result trivially extends to every less difficult case with more data or additional constraints. However, note that the extension of uniqueness to restricted measurements $I|_K$ is based on analytic continuation of the data—a very *unstable* procedure in practice.

[3] Note that this behavior of $\mathcal{D}$ is fundamentally different from that of the Fourier-transform $\mathcal{F}$, which maps constants to Dirac-deltas centered at the origin.

14.2.5.1 Uniqueness for the Linearized Model

Uniqueness for the *linearized* XPCI-model has to be shown individually. According to Sect. 14.1.2.2, it corresponds to data of the form $I_{\text{lin}} = 1 - \mathcal{D}(h) - \overline{\mathcal{D}(h)}$. Compared to (14.22), merely the quadratic term $|\mathcal{D}(o)|^2$ is omitted and $o = \exp(-h) - 1$ is replaced by $-h$ (note that this rules out phase-wrapping!). Hence, the principal uniqueness argument from [22] remains valid: the summands $\mathcal{D}(h)$ and $\overline{\mathcal{D}(h)}$ may be disentangled owing to their different "finger-prints" as entire functions:

Corollary 14.1 (Uniqueness of linearized XPCI [22]) *For any bounded domain $\Omega \subset \mathbb{R}^m$ and any $K \subset \mathbb{R}^m$ that contains an open set, the linearized forward operator $\mathcal{T}_K : L^2(\Omega) \to L^2(\mathbb{R}^m);\ h \mapsto \mathcal{T}(h)|_K$ is injective.*

14.2.5.2 Uniqueness for XPCT

By combining with standard results on uniqueness of tomographic reconstruction described by the theory of the Radon transform, the uniqueness theorems may be easily extended to XPCT. We refer to [22] for details.

14.3 Stability Theory

The uniqueness results of the preceding Sect. 14.2, suprisingly strong though they are, do not guarantee that accurate images may actually be reconstructed from holograms acquired in real-world XPCI-setups. Experimental data always contains errors due to noise and/or inaccuracies of the physical model. As detailed in Chap. 5 such data errors may lead to arbitrarily strongly corrupted images due to the phenomenon of *ill-posedness*: even if a forward model $F : X \to Y$ is injective, its inverse $F^{-1} : F(X) \to X$ may be *discontinuous* such that small perturbations in the data $g^{\text{obs}} = F(f) + \epsilon$ may be arbitrarily amplified in the reconstruction $F^{-1}(F(f) + \epsilon)$.

The aim of this section is thus to supplement the uniqueness results with an analysis of *stability*, exploring how susceptible image reconstruction is to data errors. Thereby, it sheds a light on the question which reconstructions are feasible in practice. Due to difficulties arising from nonlinearity, the stability analysis is restricted to the linearized forward models.

14.3.1 Lipschitz-Stability and its Meaning

Although other (weaker) concepts of stability are common in the field of inverse problems, the notion of *Lipschitz-stability* turns out to be most suitable for XPCI: a forward map $F : X \to Y$ between normed spaces X, Y is said to be *Lipschitz-stable* if a stability estimate of the form

$$\|F(f_1) - F(f_2)\|_Y \geq C_{\text{stab}} \|f_1 - f_2\|_X \quad \text{for all} \quad f_1, f_2 \in X \tag{14.24}$$

holds for some constant $C_{\text{stab}} > 0$. In this case, F has a *Lipschitz-continuous* inverse F^{-1}: $\|F^{-1}(g_1) - F^{-1}(g_2)\|_X \leq C_{\text{stab}}^{-1} \|g_1 - g_2\|_Y$ for all $g_1, g_2 \in F(X)$. Notably, this implies robustness to data errors: given measurements $g_\epsilon = F(f^\dagger) + \epsilon \in F(X)$, the resulting reconstruction-error is bounded by

$$\left\| f^\dagger - F^{-1}(g_\epsilon) \right\|_X = \left\| F^{-1}(F(f^\dagger)) - F^{-1}(F(g_\epsilon)) \right\|_X \leq C_{\text{stab}}^{-1} \|\epsilon\|_Y. \tag{14.25}$$

The bound (14.25) states that data errors manifest at most amplified by a finite factor C_{stab}^{-1} in the recovered object. Therefore C_{stab} should be as large as possible: if $C_{\text{stab}} \ll 1$, the error-amplification predicted by (14.25) may be too large to guarantee accurate reconstructions at realistic noise-levels $\|\epsilon\|_Y$.

Notably, for *linear* forward models $F : X \to Y$, (14.24) is equivalent to

$$C_{\text{stab}} = \inf_{f \in X, \|f\|_X = 1} \|F(h)\|_Y > 0. \tag{14.26}$$

Moreover, a linear inverse problem is *well-posed* if and only if (14.26) holds.

14.3.2 Stability for General Objects and one Hologram

Firstly, we consider the most challenging setting of reconstructing arbitrary phase- and absorption-images ϕ, μ from a single (linearized) hologram $I \approx 1 + \mathscr{T}(h)$. Stable inversion of the forward map $\mathscr{T}$ is commonly argued to be infeasible. Indeed, as seen in Sect. 14.2.1, the forward model is not even unique for general images $\phi, \mu \in L^2(\mathbb{R}^m)$, but only if ϕ, μ are compactly supported. Accordingly, we assume a *support contraint* in the following:

$$h = \mu + \mathrm{i}\phi \in L^2(\Omega) \quad \text{for some} \quad \Omega \subset \mathbb{R}^m \quad \text{bounded.} \tag{14.27}$$

14.3.2.1 Analytical Approach

Our approach to analyzing stability is ultimately based on the principle of holographic reconstruction [23], that earned DENNIS GABOR the Nobel Prize in physics in 1971. The idea is to rewrite the forward map in the form

$$-\mathscr{T}(h) = 2\mathrm{Re}\,(\mathcal{D}(h)) = \mathcal{D}(h) + \overline{\mathcal{D}(h)} = \mathcal{D}(h) + \mathcal{D}^{-1}(\overline{h}), \tag{14.28}$$

which reveals linearized XPCI data to be a superposition of a propagated image $\mathcal{D}(h)$ and the *back*-propagated *twin-image* $\overline{h}$. Applying the Fresnel-propagator $\mathcal{D}$ to

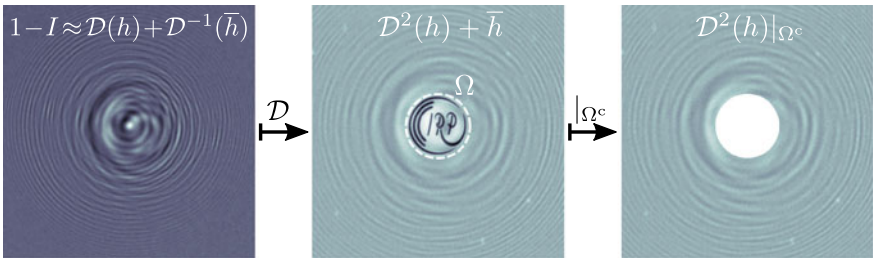

Fig. 14.2 Idea of the stability analysis of $\mathscr{T}$ [24]: by applying the propagator $\mathcal{D}$ to linear XPCI-data $I - 1 \approx \mathscr{T}(h)$, the *twin-image* $\overline{h}$ becomes sharp, see logo in central panel. By restricting to the complement of $\Omega \supset \mathrm{supp}(\overline{h})$, $\overline{h}$ is eliminated and incomplete Fresnel data $\mathcal{D}^2(h)|_{\Omega^c}$ is obtained (right panel). Images show real parts of images computed from a hologram (left panel) acquired at GINIX [25, 26], P10-beamline, DESY

a hologram thus recovers the twin-image $\overline{h}$, perturbed by a fringe-pattern originating from the doubly propagated image $\mathcal{D}^2(h)$:

$$-\mathcal{D}\big(\mathscr{T}(h)\big) = \mathcal{D}^2(h) + \overline{h}, \tag{14.29}$$

This is Gabor's original idea of *holographic reconstruction*, which is illustrated in the first and second panel of Fig. 14.2 for a real-data example.

For stability analysis, we use the idea in a converse manner. By the constraint $h \in L^2(\Omega)$, the sharp twin-image (the valuable part ins Gabor's eyes!) can be eliminated from (14.29) by restricting to the complement Ω^c of Ω:

$$-\mathcal{D}\big(\mathscr{T}(h)\big)|_{\Omega^c} = \mathcal{D}^2(h)|_{\Omega^c} + \overline{h}|_{\Omega^c} \overset{\mathrm{supp}(\overline{h})\subset\Omega}{=} \mathcal{D}^2(h)|_{\Omega^c}. \tag{14.30}$$

By (14.30), we are left with *incomplete* (but phased!) Fresnel-data $\mathcal{D}^2(h)|_{\Omega^c}$. Notably, to this point, only *stable* operations have been applied to the XPCI-data, which do not amplify data errors in L^2-norm: for any $g \in L^2(\mathbb{R}^m)$, it holds that $\|\mathcal{D}(g)|_{\Omega^c}\|_{L^2} \le \|g\|_{L^2}$. When applied to (14.30) this bound yields

$$\|\mathscr{T}(h)\|_{L^2} \ge \big\|\mathcal{D}\big(\mathscr{T}(h)\big)|_{\Omega^c}\big\|_{L^2} = \big\|\mathcal{D}^2(h)|_{\Omega^c}\big\|_{L^2}. \tag{14.31}$$

Finally, by employing the alternate form (14.20) of $\mathcal{D}$, the Fresnel-data on the r.h.s. of (14.31) may be identified with incomplete *Fourier*-data:

$$\|\mathscr{T}(h)\|_{L^2} \ge \big\|\mathcal{D}^2(h)|_{\Omega^c}\big\|_{L^2} = \|\mathcal{F}(\tilde{h})|_{\Omega_\mathfrak{f}^c}\|_{L^2} \tag{14.32}$$

with $\tilde{h} = n_{\mathfrak{f}/2} \cdot h$ and $\Omega_\mathfrak{f} := \{\boldsymbol{x} \in \mathbb{R}^m : (2/\mathfrak{f}) \cdot \boldsymbol{x} \in \Omega\}$.

14.3.2.2 Stability Bound

Since $\|\tilde{h}\|_{L^2} = \|h\|_{L^2}$, the bound (14.32) can be regarded as a *relative* stability estimate: recovering an image $h \in L^2(\Omega)$ from XPCI-data $\mathscr{T}(h)$ is *at least as stable* as the reconstruction of $\tilde{h} \in L^2(\Omega)$ from Fourier-data outside the domain $\Omega_\mathfrak{f}$. Reconstruction from incomplete Fourier-data in turn is a well-studied problem: an *uncertainty principle* from [27] implies that Lipschitz-stability holds, $\|\mathcal{F}(\tilde{h})|_{\Omega_\mathfrak{f}^c}\| \geq C_{\text{stab}}^{\text{gen}} \|\tilde{h}\|$ for some $C_{\text{stab}}^{\text{gen}} > 0$, provided that Ω is bounded along at least one dimension. For rectangular domains Ω, the stability-constant $C_{\text{stab}}^{\text{gen}}$ may be expressed in terms of the principal eigenvalue of a compact selfadjoint operator, for which asymptotics are derived in [28]. Via (14.32), these results yield stability estimates for linearized XPCI:

Theorem 14.2 (Stability estimate for general images [24]) *Let* $\Omega = [-\frac{1}{2}; \frac{1}{2}]^m$. *Then*

$$C_{stab}^{gen}(\Omega, \mathfrak{f}) := \inf_{h \in L^2(\Omega), \|h\|=1} \|\mathscr{T}(h)\| > 0 \tag{14.33}$$

i.e. the reconstruction of images h with support in Ω *from linearized XPCI-data is well-posed. For* $\mathfrak{f} \to \infty$, *the stability constant satisfies the bound*

$$C_{stab}^{gen}(\Omega, \mathfrak{f}) \geq m^{\frac{1}{2}} (2\pi\mathfrak{f})^{\frac{1}{4}} \left(1 - \frac{3}{8\mathfrak{f}} + \mathcal{O}\left(\mathfrak{f}^{-2}\right)\right) \exp\left(-\mathfrak{f}/8\right). \tag{14.34}$$

While Theorem 14.2 only gives a *worst-case* bound on the data-contrast $\|\mathscr{T}(h)\|/\|h\|$ over all images h, the result may be sharpened considerably, as detailed in [24]: for any $h \in L^2(\Omega)$, an individual lower bound for $\|\mathscr{T}(h)\|$ may be given based on the eigenvalues from [28] and the images that minimize $\|\mathscr{T}(h)\|/\|h\|$ may be characterized in terms of the associated eigenmodes.

14.3.2.3 Stability in a Practical Sense?

Numerical computations in [24] indicate that the bound (14.34) is quite sharp. While this is good news for a (pure) mathematician, it is bad news from an applied perspective: the predicted (quasi) exponential decay $C_{\text{stab}}^{\text{gen}}(\Omega, \mathfrak{f}) \sim \exp(\mathfrak{f}/8)$ implies that the constant quickly becomes very small for larger values of $\mathfrak{f}$, e.g. $C_{\text{stab}}^{\text{gen}}(\Omega, \mathfrak{f}) \lesssim 10^{-5}$, for $\mathfrak{f} \gtrsim 100$. Notably, $\mathfrak{f} = kb^2/d$ is the modified Fresnel-number associated with the width of the support-domain Ω, i.e. with the diameter of the imaged sample.[4] In typical XPCI-experiments at synchrotrons, one has $10^2 \lesssim \mathfrak{f} \lesssim 10^5$, so that Theorem 14.2 only guarantees stability *in practice* for imaging settings at the lower end of typical Fresnel-numbers.

[4]The lateral lengthscale b associated with $\mathfrak{f}$ is implicitly fixed to the width of Ω by assuming the latter to be 1 in Theorem 14.2, as will also be done in all subsequent results.

Notably, this is in line with empirics: after all, independent reconstruction of phase- and absorption-image ϕ and μ from a single hologram, as analyzed here, is widely considered as infeasible by practioners. It is thus highly surprising in the first place that the problem is technically *well-posed* at all.

14.3.2.4 Extension to Other Domains

Theorem 14.2 seemingly only applies to a very particular choice of the domain $\Omega \subset \mathbb{R}^m$. Yet, it may be readily generalized via the following properties:

- *Translation- and rotation-invariance*: As the map $\mathscr{T}$ is invariant under shifts and/or rotations of the coordinates, it holds that $C^{\text{gen}}_{\text{stab}}(\tilde{\Omega}, \mathfrak{f}) = C^{\text{gen}}_{\text{stab}}(\Omega, \mathfrak{f})$ whenever $\tilde{\Omega}$ is a shifted and/or rotated version of $\Omega \subset \mathbb{R}^m$.
- *Monotonicity*: $C^{\text{gen}}_{\text{stab}}(\Omega_1, \mathfrak{f}) \geq C^{\text{gen}}_{\text{stab}}(\Omega_2, \mathfrak{f})$ for any $\Omega_1 \subset \Omega_2 \subset \mathbb{R}^m$.
- *Scaling*: $C^{\text{gen}}_{\text{stab}}(r \cdot \Omega, \mathfrak{f}) \geq C^{\text{gen}}_{\text{stab}}(\Omega, r^2\mathfrak{f})$ for any $\Omega \subset \mathbb{R}^m$ and $r > 0$.

Analogous properties hold for the stability constants in Sect. 14.3.3.

14.3.3 Homogeneous Objects and Multiple Holograms

In most practical works, one aims to stabilize image reconstruction in XPCI by one of the following approaches (often both, actually):

1. Impose a homogeneity-constraint, e.g. assuming a pure phase object $h = \mathrm{i}\phi$ if absorption is negligible ($\mu \approx 0$), see Sect. 14.1.2.3.
2. Reconstruct from more than one hologram, see Sect. 14.1.2.4.

According to Sect. 14.2.1, uniqueness then also holds without support constraints, but image reconstruction is still *ill-posed* in general: the associated forward maps $\mathscr{S}_\nu : L^2(\mathbb{R}^m) \to L^2(\mathbb{R}^m)$ and $\mathscr{T}^{(\mathfrak{f}_1,\dots,\mathfrak{f}_\ell)} : L^2(\mathbb{R}^m) \to L^2(\mathbb{R}^m)^\ell$ do not have a bounded inverse due to zeros of the CTFs.

When both homogeneity- and support constraints can be assumed, well-posedness holds true with an improved stability constant compared to (14.34):

Theorem 14.3 (Stability estimate for homogeneous objects [24]) *Let $\Omega \subset \mathbb{R}^m$ be a ball of diameter 1, w.l.o.g. $\Omega = \{\boldsymbol{x} \in \mathbb{R}^m : |\boldsymbol{x}| \leq \frac{1}{2}\}$. Then*

$$\begin{aligned} C^{hom}_{stab}(\Omega, \mathfrak{f}, \nu) &:= \inf_{\varphi \in L^2(\Omega), \|\varphi\|_{L^2}=1} \|\mathscr{S}_\nu(\varphi)\|_{L^2} \\ &\geq \max\left\{\min\left\{c_1, c_2\mathfrak{f}^{-1}\right\}, \min\left\{c_3\nu, c_4\mathfrak{f}^{-\frac{1}{2}}\right\}\right\} \end{aligned} \tag{14.35}$$

for some constants $c_j > 0$ that depend only on m.

By Theorem 14.3, the original decay $C_{\text{stab}}^{\text{gen}} \sim \exp(-\mathfrak{f}/8)$ of the stability constant as $\mathfrak{f} \to \infty$ improves to $C_{\text{stab}}^{\text{hom}}(\Omega, \mathfrak{f}, \nu) \sim \mathfrak{f}^{-\gamma}$ with $\gamma = 1$ for $\nu = 0$ and $\gamma = 1/2$ for $\nu > 0$. This ensures *practical* stability also at larger Fresnel-numbers.

A similar improvement applies for the reconstruction of general objects (no homogeneity-constraint) from *two* holograms:

Theorem 14.4 (Stability estimate for two holograms [24]) *Let* $\mathscr{T}^{(\mathfrak{f}_1,\mathfrak{f}_2)} : h \mapsto (\mathscr{T}^{(\mathfrak{f}_1)}(h), \mathscr{T}^{(\mathfrak{f}_2)}(h))$ *denote the linearized XPCI-model for two holograms at Fresnel-numbers* $\mathfrak{f}_1 \neq \mathfrak{f}_2$ *(see Sect. 14.1.2.4). Let* $\mathscr{S}_0^{(\mathfrak{f}_-)}$ *be the forward map from Theorem 14.3 for* $\nu = 0$ *and* $\mathfrak{f} = \mathfrak{f}_- := |\mathfrak{f}_1^{-1} - \mathfrak{f}_2^{-1}|^{-1}$. *Then*

$$\left\| \mathscr{T}^{(\mathfrak{f}_1,\mathfrak{f}_2)}(h) \right\|_{L^2} \geq 2^{-\frac{1}{2}} \left\| \mathscr{S}_0^{(\mathfrak{f}_-)}(h) \right\|_{L^2} \qquad \text{for all} \qquad h \in L^2(\mathbb{R}^m). \tag{14.36}$$

In particular, for any support-domain $\Omega \subset \mathbb{R}^m$, *the following stability estimate holds true:*

$$C_{stab}^{two}(\Omega, \mathfrak{f}_1, \mathfrak{f}_2) := \inf_{\substack{h \in L^2(\Omega) \\ \|h\|_{L^2}=1}} \left\| \mathscr{T}^{(\mathfrak{f}_1,\mathfrak{f}_2)}(h) \right\|_{L^2} \geq 2^{-\frac{1}{2}} C_{stab}^{hom}(\Omega, \mathfrak{f}_-, 0). \tag{14.37}$$

Note that the r.h.s. of the stability bound (14.37) increases with the difference $\mathfrak{f}_-^{-1}$ between the reciprocal Fresnel-numbers $\mathfrak{f}_1^{-1}, \mathfrak{f}_2^{-1}$. Improved stability is thus guaranteed only if $\mathfrak{f}_1$ and $\mathfrak{f}_2$ differ strongly, i.e. if the two holograms are acquired in significantly different experimental setups.

14.3.3.1 Order-Optimality

For $\nu = 0$, it can be shown that the $\sim \mathfrak{f}^{-1}$ order of the decay in Theorem 14.3 cannot be improved: for a fixed bounded domain $\Omega \subset \mathbb{R}^m$ with non-empty interior, there exists a constant $c_{\max}(\Omega) > 0$ such that

$$C_{\text{stab}}^{\text{hom}}(\Omega, \mathfrak{f}, 0) \leq c_{\max}(\Omega)\mathfrak{f}^{-1}. \tag{14.38}$$

This is a consequence of the bound $\|\mathscr{S}_0(\varphi)\|_{L^2} \leq 1/\mathfrak{f}\|\Delta\varphi\|_{L^2}$ where Δ is the Laplacian, which in turn follows from $|s_0(\boldsymbol{\xi})| \leq \boldsymbol{\xi}^2/(2\mathfrak{f})$ for all $\boldsymbol{\xi} \in \mathbb{R}^m$.

Notably, better rates do not even hold in a setting with multiple holograms: for any Fresnel-numbers $\mathfrak{f}_1, \ldots, \mathfrak{f}_\ell$, it holds by a similar argument that

$$\inf_{\varphi \in L^2(\Omega), \|\varphi\|_{L^2}=1} \|\mathscr{S}_0^{(\mathfrak{f}_1,\ldots,\mathfrak{f}_\ell)}(\varphi)\|_{L^2} \leq c_{\max}(\Omega) \left(\sum_{i=1}^{\ell} \mathfrak{f}_i^{-2} \right)^{\frac{1}{2}}. \tag{14.39}$$

The reason for this surprising negative result on the benefit of multiple holograms is that the CTFs $s_0^{(\mathfrak{f}_i)}(\boldsymbol{\xi}) = \sin(\boldsymbol{\xi}^2/(2\mathfrak{f}_i))$ all share a second order zero at $\boldsymbol{\xi} = 0$. This

corresponds to the well-known *low-frequency instability* of XPCI that gives rise to the proven $\mathfrak{f}^{-1}$-rates of the stability constant.

14.3.3.2 Numerical Stability Computations

Other than for the setting in Theorem 14.2, the prediction (14.35) for the stability constant $C_{\text{stab}}^{\text{hom}}$ (and thus for $C_{\text{stab}}^{\text{two}}$) is far from sharp if the analytical bounds on the constants c_j from [24] are inserted. Sharp values of $C_{\text{stab}}^{\text{hom}}$ may however be computed numerically by approximating the minimum singular value of the operator $\mathscr{S}_\nu$ via techniques presented in [29, Sect. 3.4].

14.3.4 Extensions

14.3.4.1 Phase Contrast Tomography

Although the physical setting of XPCI corresponds to $m = 2$ dimensions, the stability results in Theorems 14.2 to 14.4 have been formulated for arbitrary m. As a benefit, stability may be readily extended to XPCT: for the considered linearized forward models, XPCT data is of the form $I_{\boldsymbol{\theta}} - 1 = T\,(\mathscr{P}_{\boldsymbol{\theta}}(f))$ for $T \in \{\mathscr{T}, \mathscr{S}_\nu\}$ and incident directions $\boldsymbol{\theta} \in \Theta \subset \mathbb{S}^2$, compare Sect. 14.1.3. As noted in [30, 31], the order of the projector $\mathscr{P}_{\boldsymbol{\theta}}$ and T may be interchanged:

$$I_{\boldsymbol{\theta}} - 1 = T\,(\mathscr{P}_{\boldsymbol{\theta}}(f)) = \mathscr{P}_{\boldsymbol{\theta}}\left(T^{(3\mathrm{d})}(f)\right), \tag{14.40}$$

where $T^{(3\mathrm{d})} \in \{\mathscr{T}^{(3\mathrm{d})}, \mathscr{S}_\nu^{(3\mathrm{d})}\}$ is the equivalent of T in $m = 3$ dimensions.

As detailed in [29, Sect. 3.3], the relation (14.40) allows to express stability of linearized XPCT via known results for tomographic reconstruction, combined with stability bounds for $\mathscr{T}^{(3\mathrm{d})}, \mathscr{S}_\nu^{(3\mathrm{d})} : L^2(\Omega) \to L^2(\mathbb{R}^3)$ where $\Omega \subset \mathbb{R}^3$. Stability then depends on a *three-dimensional* support constraint $\operatorname{supp}(\beta + \mathrm{i}\delta) \subset \Omega \subset \mathbb{R}^3$ for the imaged sample's refractive index.

14.3.4.2 Imaging with Finite Detectors

There are a number of idealizing assumptions underlying to the obtained stability estimates: in addition to the neglected nonlinearity and idealizations in the basic physical model such as full coherence, it has also been assumed that the hologram I is measured in the whole detector-plane in Fig. 14.1. Due to the finite size of real-world detectors (and—more fundamentally—the finite width of illuminating X-ray beams), however, only restrictions $I|_K$ to some bounded domain K are available in practice.

According to Theorem 14.1, such restricted data has *no* impact on *uniqueness* (if K contains an open set). The situation is quite different in terms of *stability*, as analyzed in [32]: for any bounded $K \subset \mathbb{R}^m$—however large—the inverse problem of XPCI becomes *severely ill-posed*, i.e. Lipschitz-stability is lost so that data errors may severely corrupt the reconstructed images. Yet, it is also proven in [32] that the situation may be repaired by restricting to images $h = \mu + \mathrm{i}\phi$ of *finite resolution* (smoothness constraint in the sense of Sect. 14.1.1.1): by imposing that the h are B-splines on a Cartesian grid of sufficiently large spacing $r(\Omega, K, \mathfrak{f}) > 0$ (i.e. *pixelated* images in some sense), Lipschitz-stability can be restored in the finite-detector setting. Physically, the necessity of such a restriction corresponds to a *resolution limit* that arises due to the finite numerical aperture associated with the detector size.

14.4 Regularized Newton Methods for XPCI

The following section considers regularized Newton-type methods for image reconstruction in XPCI. The proposed algorithm is motivated by the theoretical insights gained from Sects. 14.2 and 14.3.

14.4.1 Motivation

14.4.1.1 Significance of Constraints

The stability results of Sect. 14.3 heavily rely on *support constraints*—without such, XPCI is ill-posed or even non-unique. To guarantee stability in practice, image reconstruction methods must thus be able to exploit support-knowledge. Also other types of a priori knowledge (see Sect. 14.1.1.1) are known to be beneficial. In particular, imposing *non-negativity* often has a similar stabilizing effect as support constraints.

14.4.1.2 Necessity of Iterative Methods

By far the most commonly used reconstruction method for XPCI at synchrotrons is direct CTF-inversion, as presented in Sect. 2.3. Within the notation of this chapter, the approach corresponds to quadratic Tikhonov regularization applied to the linearized forward maps $\mathscr{S}_\nu^{(\mathfrak{f}_1,\dots,\mathfrak{f}_\ell)}$ or $\mathscr{T}^{(\mathfrak{f}_1,\dots,\mathfrak{f}_\ell)}$. Owing to the *linearity* and *translation-invariance* of these maps, the reconstruction may be implemented via a multiplication in Fourier-space (deconvolution), which renders the approach computationally fast.

However, direct CTF-inversion is incompatible with the above constraints:

- Support constraints $\mathrm{supp}(h) \subset \Omega$ for $\Omega \subsetneq \mathbb{R}^m$ break translation-invariance
- Non-negativity is a *nonlinear* constraint: any reconstruction imposing it depends nonlinearly on the data $I - 1$—even for linear forward models!

In either case, reconstruction may thus no longer be achieved by deconvolution. Thus, *iterative* algorithms have to be applied to impose support- and/or nonnegativity-constraints in lack of efficient direct reconstruction formulas.

14.4.1.3 XPCI Beyond Linear Models

Although the linear CTF-model of XPCI has a surprisingly large regime-of-validity, there are settings where linear image reconstruction induces severe artifacts arising from the neglected nonlinearity, as demonstrated in Sect. 13.3. Reconstruction algorithms based on the full nonlinear XPCI-model are thus preferable in principle. The main obstacle in using such is that direct inversion formulas for the nonlinear model are not known. However, when iterative methods are needed anyway (Sect. 14.4.1.2), nonlinear forward maps cause little additional difficulty.

14.4.2 Reconstruction Method

In the following, we propose a reconstruction algorithm that meets the requirements discussed in Sect. 14.4.1. Details can be found in [33].

By choosing $F : X \to L^2(\mathbb{R}^m) \in \{\mathscr{N}, \mathscr{N}_\nu\}$ with $X = L^2(\Omega, (\mathbb{R}))$ for $\Omega \subset \mathbb{R}^m$, optional homogeneity- and/or support constraints are incorporated in the forward operator F. Consequently, such constraints are imposed *automatically* if image reconstruction in XPCI is performed by inverting F via any generic regularization method for inverse problems, see Chap. 5. In order to exploit Fréchet-differentiability of $\mathscr{N}$ (see Sect. 14.1.2.1) and the comparably moderate nonlinearity of XPCI, we choose regularized Newton methods as introduced in Chap. 5:

$$h_{k+1} \in \operatorname{argmin}_{h \in X} \left\| F(h_k) + F'[h_k](h - h_k) - (I^{\mathrm{obs}} - 1) \right\|_{L^2}^2 + \alpha_k \|h - h_0\|_{H^s}^2 + \mathcal{R}_{\geq 0}(h, h_k). \tag{14.41}$$

for $k = 0, 1, \ldots, k_{\mathrm{stop}}$, with initial guess $h_0 \in X$ (usually $h_0 = 0$), observed (noisy) hologram(s) I^{obs} and regularization parameters $\alpha_k > 0$.

Note that we use a standard squared L^2-norm as a *data-fidelity* term in (14.41), in lack of an accurate model for the data error statistics in flat-field corrected holograms. The squared Sobolev-term $\alpha_k \|h - h_0\|_{H^s}^2$ ($\|f\|_{H^s}^2 := \|(1 + \boldsymbol{\xi}^2)^{s/2} \cdot \mathcal{F}(f)\|_{H^s}^2$) imposes tunable (by the choice of $s \geq 0$) smoothness of the iterates h_k and acts as a regularizer. Finally, $\mathcal{R}_{\geq 0}(h, h_k)$ is a quadratic penalty term that is designed to

correct negative values of $\mathrm{Re}(h_k)$ or $\mathrm{Im}(h_k)$ in the subsequent iterate h_{k+1}, see [33] for details.

In the numerical algorithm, a discretized analogue of the quadratic minimization problem in (14.41) is solved for images $\boldsymbol{h}_* \in \mathbb{C}^N$, data $\boldsymbol{I}^{\mathrm{obs}} \in \mathbb{R}^M$ and forward map $F_{\mathrm{dis}} : \mathbb{C}^N \to \mathbb{R}^M$, via a conjugate-gradient method. The α_k and k_{stop} are chosen in a widely automated fashion, as detailed in [33].

14.4.3 Reconstruction Example

We assess the capabilities of the proposed method by reconstructing phase ϕ and absorption μ as independent parameters from a single simulated noisy hologram, which is shown in Fig. 14.3a. The considered test case is detailed in [33], where also a real-data example is considered for an analogous setting.

The true phase-image ϕ (Fig. 14.3b) is given by a bulk disk of magnitude 0.2, whereas the true absorption-image $0 \leq \mu \leq 0.02$ shows a logo-structure (Fig. 14.3c). Accordingly, *no* homogeneity-constraint is applicable so that the test-case is situated in the most challenging, unstable setting of XPCI, which has been analyzed in Sect. 14.3.2. In particular, recall that image reconstruction is non-unique without exploiting further constraints.

The data is reconstructed using the regularized Newton method from Sect. 14.4.2, imposing non-negativity of ϕ and μ as well as support constraint, allowing nonzero values of ϕ, μ only within the circular region marked by the blue dashed line in Fig. 14.3b, c. The reconstructed images in Fig. 14.3d, e show that the proposed method correctly attributes the disk-structure to the phase-image ϕ and the logo-pattern to μ, without visible signs of "mixing things up". The overall lower reconstruction-quality in μ compared to ϕ is due to the lower signal-to-noise in this parameter, as a realistically low absorption-refraction-ratio $\beta/\delta \leq 0.1$ has been assumed in the test case.

Now why does reconstruction of both ϕ and μ from a single hologram work here, contrary to the usual experience? The diameter of the circular support corresponds to a relatively low (modified) Fresnel-number $\mathfrak{f} \approx 87$. According to the analysis in Sect. 14.3.2, this ensures stability of image reconstruction, as is discussed to greater detail in [33] and [24, Sect. 6]. By its ability to impose support constraints (and non-negativity), the proposed Newton-type method allows to exploit this theoretical stability in practice.

14.5 Regularized Newton-Kaczmarz-SART for XPCT

In the final section, we present a Newton-type reconstruction method for X-ray phase contrast *tomography* (XPCT) that is a compromise between flexibility w.r.t. a priori constraints and computational performance. We note that the method is an

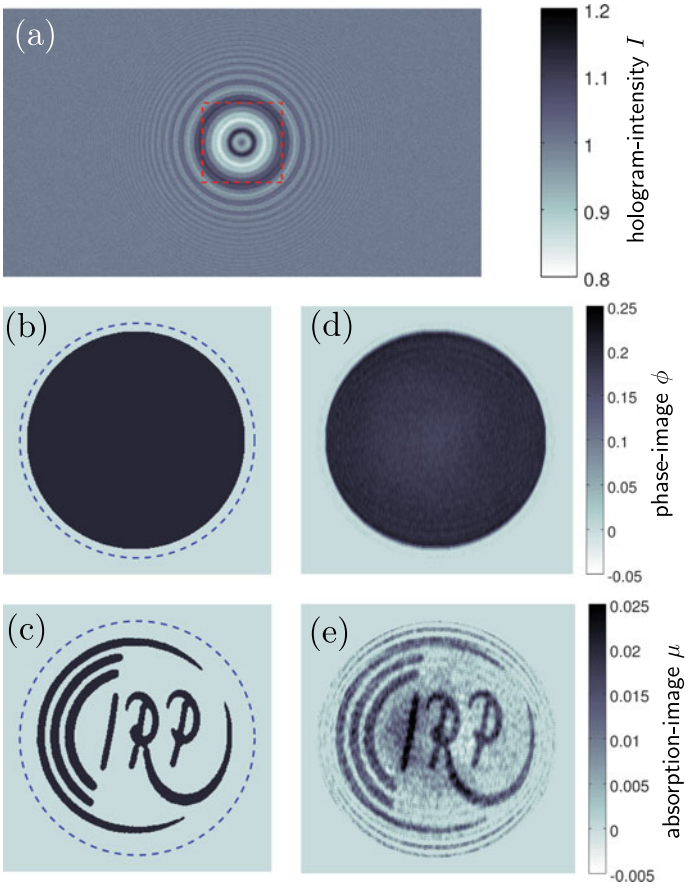

Fig. 14.3 Reconstruction of a general image $h = \mu + \mathrm{i}\phi$ from a single simulated hologram by a regularized Newton method (test case from [33]). **a** Hologram of size 1920×1080. **b**, **c** True images ϕ and μ (zooms to the relevant region, that is marked by a red-dashed line in (**a**)). **d**, **e** Reconstructed images ϕ and μ, obtained by imposing non-negativity and *support* of ϕ, μ within the circular region bounded by the blue-dashed line in (**b**), (**c**)

all-at-once approach, as also proposed in [30, 31, 34]: the 3D-object parameters δ, β are recovered directly from the full tomographic hologram-series, instead of first reconstructing 2D-images ϕ, μ for each hologram individually. Thereby, *tomographic consistency* is imposed as an additional constraint in image reconstruction, compare Sect. 14.1.1.1.

By replacing $F \in \{\mathcal{N}, \mathcal{N}_\nu\}$ with the corresponding *tomographic* forward operator from Sect. 14.1.3, $F_{\mathrm{PCT}} : X \to L^2(\mathbb{R}^2)^t;\ \ f \mapsto (F(\mathscr{P}_{\theta_j}(f)))_{j=1}^t$ with $X = L^2(\Omega, (\mathbb{R}))$, $\Omega \subset \mathbb{R}^3$, the regularized Newton method from Sect. 14.4.2 may be readily adapted to solve the inverse problem of XPCT:

$$F_{\mathrm{PCT}}(f) \approx (I_{\theta_j}^{\mathrm{obs}} - 1)_{j=1}^{t} \quad \text{for} \quad f = k\beta + \mathrm{i}k\delta \in X. \tag{14.42}$$

This is done in [2]. Yet, typical problem-sizes in XPCT with $\sim 10^9$ dimensions of the discretized object- and data-space, are too large for this approach to be competitive in terms of computation times and memory requirements.

As a remedy, we supplement the approach with a *Kaczmarz-type* strategy that exploits the block-structure of the XPCT-problem (14.42). The idea is to cyclically perform regularized Newton-steps w.r.t. the small sub-problems $I_{\theta_j}^{\mathrm{obs}} - 1 \approx F(\mathscr{P}_{\theta_j}(f))$ defined by the measured holograms $I_{\theta_j}^{\mathrm{obs}}$ under the different tomographic incident directions θ_j:

$$\begin{aligned} f_{k+1} \in \operatorname{argmin}_{f \in X} \Big\| F(\mathscr{P}_{\theta_{j_k}}(f_k)) + F'[\mathscr{P}_{\theta_{j_k}}(f_k)]\mathscr{P}_{\theta_{j_k}}(f - f_k) - \big(I_{\theta_{j_k}}^{\mathrm{obs}} - 1\big)\Big\|^2 \\ + \alpha\big((1-\gamma)\,\|f - f_k\|_{L^2}^2 + \gamma\,\|\nabla(f - f_k)\|_{L^2}^2\big) \end{aligned} \tag{14.43}$$

for $k = 0, 1, \ldots, tn_{\mathrm{stop}} - 1$ with $n_{\mathrm{stop}} \in \mathbb{N}$. The parameters $\alpha > 0, 0 \le \gamma \le 1$ control the regularization and smoothing w.r.t. the preceding iterate f_k.

Iterations of the form (14.43) are known as *regularized Newton-Kaczmarz* [35]. The advantage compared to *bulk* (i.e. non-Kaczmarz-)methods is that the operator-blocks $f \mapsto F(\mathscr{P}_{\theta_j}(f))$ require much less computations to evaluate than the total XPCT operator F_{PCT}, which permits efficient computation of the iterates (14.41). Moreover, Kaczmarz-type methods often exhibit fast initial convergence, typically reaching a good reconstruction already after one or two *cycles* over the data, i.e. for $n_{\mathrm{stop}} \in \{1, 2\}$. To promote convergence, the processing order $\{j_1, j_2, \ldots\} \subset \{1, \ldots, t\}$ of the data-blocks should be chosen such that subsequently fitted directions $\theta_{j_k}, \theta_{j_{k+1}}$ differ as strongly as possible, which we achieve by following a "multi-level-scheme" from [36].

14.5.1 Efficient Computation by Generalized SART

Although the processed *data*-size is reduced by the Kaczmarz-strategy, the iterates (14.41) still involve a minimization problem on a high-dimensional space of 3D-objects f. Moreover, if the minimization is performed iteratively, each iteration requires evaluations of the (discretized) projector $\mathscr{P}_{\theta_{j_k}}$ and its adjoint $\mathscr{P}_{\theta_{j_k}}^*$, the *back*-projector, both of which typically amount to much higher computational costs than evaluating the XPCI forward map F.[5]

Both computational issues can be resolved by computing the iterates (14.41) via a *generalized SART*[6] (GenSART-) scheme, as introduced in [38] for a much more general class of tomographic Kaczmarz-iterations:

[5] For images of size $N \times N$, the discretized forward maps $F = \mathscr{N}^{(\mathrm{f}_1, \ldots, \mathrm{f}_\ell)}$ may be evaluated in $\mathcal{O}(\ell N^2 \log N)$ operations, while (back-)projecting 3D-arrays of size $N \times N \times N$ is $\mathcal{O}(N^3)$.

[6] "SART" refers to the simultaneous algebraic reconstruction technique from [37].

GenSART for Newton-Kaczmarz-iterations:

1. Forward-projection: $p_k := \mathscr{P}_{\boldsymbol{\theta}_{j_k}}(f_k)$
2. Optimization in *projection-space* ($u_j = \mathscr{P}_{\boldsymbol{\theta}_j}(\mathbf{1}_\Omega)$):

$$\begin{aligned}\Delta p_k \in \operatorname{argmin}_{p\in L^2(\mathbb{R}^2,(\mathbb{R}))} &\|F(p_k) + F'[p_k](u_{j_k}\cdot p) - (I^{\text{obs}}_{\boldsymbol{\theta}_{j_k}} - 1)\|^2_{L^2} \\ &+ \alpha\big((1-\gamma)\|u_{j_k}^{1/2}\cdot p\|^2_{L^2} + \gamma\|u_{j_k}^{1/2}\cdot \nabla p\|^2_{L^2}\big) \qquad (14.44)\end{aligned}$$

3. Back-projection update: $f_{k+1} = f_k + \mathscr{P}^*_{\boldsymbol{\theta}_{j_k}}(\Delta p_k)$

The main benefit of the approach is that the required minimization is cast to *projection-space*, i.e. no longer needs to be solved on a high-dimensional space of 3D-objects but merely on 2D-*images*. Moreover, the whole scheme requires only a single evaluation of $\mathscr{P}_{\boldsymbol{\theta}_{j_k}}$ (1.) and its adjoint $\mathscr{P}^*_{\boldsymbol{\theta}_{j_k}}$ (3.), whereas the optimization (2.) does not involve any of these costly operations anymore.

As is standard for Kaczmarz-type methods, non-negativity of the iterates f_{k+1} (in real- and imaginary part) may be imposed by adding a final step to the GenSART-scheme: $f_{k+1,\geq 0} = \max\{0, \operatorname{Re}(f_{k+1})\} + \mathrm{i}\max\{0, \operatorname{Im}(f_{k+1})\}$.

14.5.2 Parallelization and Large-Scale Implementation

Regularized Newton-Kaczmarz, computed via GenSART-schemes, is well-suited for large-scale computations and can be efficiently implemented in a parallelized manner. While we refer to [29, Sect. 6.3] for a detailed discussion, we mention the most important aspects here:

- *Low memory requirements*: if the back-projection update (3.) (as well as the optional non-negativity projection) is implemented as an *in-place* operation, only a single 3D-array (storing $f_0, f_1, (f_{1,\geq 0},) f_2, \ldots$) needs to be kept in memory throughout the whole Newton-Kaczmarz-reconstruction.
- *Parallelized optimization*: as the optimization-step (2.) works on *2D*-images only, its memory-requirements are low enough to be performed on a single graphical processing unit (GPU) even for large-scale data. This permits efficient parallized implementation of this step.
- *Parallelized 3D-computations*: The only operations on the 3D-objects f_k are forward- and back-projections $\mathscr{P}_{\boldsymbol{\theta}_{j_k}}$, $\mathscr{P}^*_{\boldsymbol{\theta}_{j_k}}$ and pointwise arithmetics. All of these can be easily parallelized at low communication requirements between the different processors. In fact, it is possible to implement GenSART-schemes in a distributed manner: the object-iterates f_k may be split into chunks, that are stored

and managed by dedicated machines throughout the whole reconstruction. This property allows to run Newton-Kaczmarz reconstructions efficiently on multiple GPUs.

14.5.3 Reconstruction Example

We assess the Newton-Kaczmarz method for XPCT-data of freeze-dried *Deinococcus radiodurans* bacteria. The experimental data set, acquired with the GINIX setup from Chap. 3, is composed of 641 holograms of size 2048×2048 at tomographic incident angles $\theta = 0°, 0.25°, \ldots, 119°, 139°, 139.25°, \ldots, 180°$ (one hologram per angle). 2D orthoslices of the 3D tomographic data (two spatial and one angular dimension) are shown in Fig. 14.4a–c, emphasizing the missing data between $\theta = 119°$ and $\theta = 139°$.

The biological sample constitutes a *pure phase object* to good approximation, i.e. vanishing absorption $\beta = 0$ may be assumed. Moreover, the sample is localized in a small subdomain of the imaged 2048×2048-sized field-of-view, as can be seen from Fig. 14.4a–c, i.e. support constraints may be imposed.

For comparison, we reconstruct the XPCT-data with different methods:

1. CTF+FBP: direct CTF-inversion for each hologram, followed by filtered back-projection applied to the recovered projections of δ.
2. Linear Kaczmarz: reconstruction by (14.43) over a single cycle $n_{\text{stop}} = 1$, using the *linearized* XPCI-model $F = \mathscr{S}_0$. Non-negativity of the reconstructed δ and support in a centered cube of 512^3 voxels is imposed.
3. Newton-Kaczmarz: same as (2.), but with the *nonlinear* model $F = \mathscr{N}_0$.

2D orthoslices through the reconstructed $512 \times 512 \times 512$ volumes are plotted in Fig. 14.4d–l. We note the following observations:

- The additional constraints exploited in "Linear Kaczmarz" compared to "CTF+FBP" widely eliminate low-frequency background-artifacts (compare Fig. 14.4e–h) and thereby enable *quantitatively* correct reconstructions δ.
- Though the sample-induced phase shifts are moderate, $\phi_{\boldsymbol{\theta}} = k\mathscr{P}_{\boldsymbol{\theta}}(\delta) \lesssim 1$, going over to the nonlinear XPCI-model has significant effects: especially in Fig. 14.4h, it can be seen that using the linearized model causes artificial distortions in the recovered object-density compared to the nonlinear Newton-Kaczmarz-reconstruction in Fig. 14.4i–l.

Accordingly, both the nonlinearity and the ability to exploit a priori constraints of the proposed Newton-Kaczmarz method turn out to be vital here to accurately reconstruct the anticipated 3D structure of the imaged bacteria[7]: cytoplasm with blob-shaped inclusions containing the DNA, where each of the two compounds is of approximately uniform density.

[7] The additional object in the top-left of Fig. 14.4e, h, k is a contaminant particle.

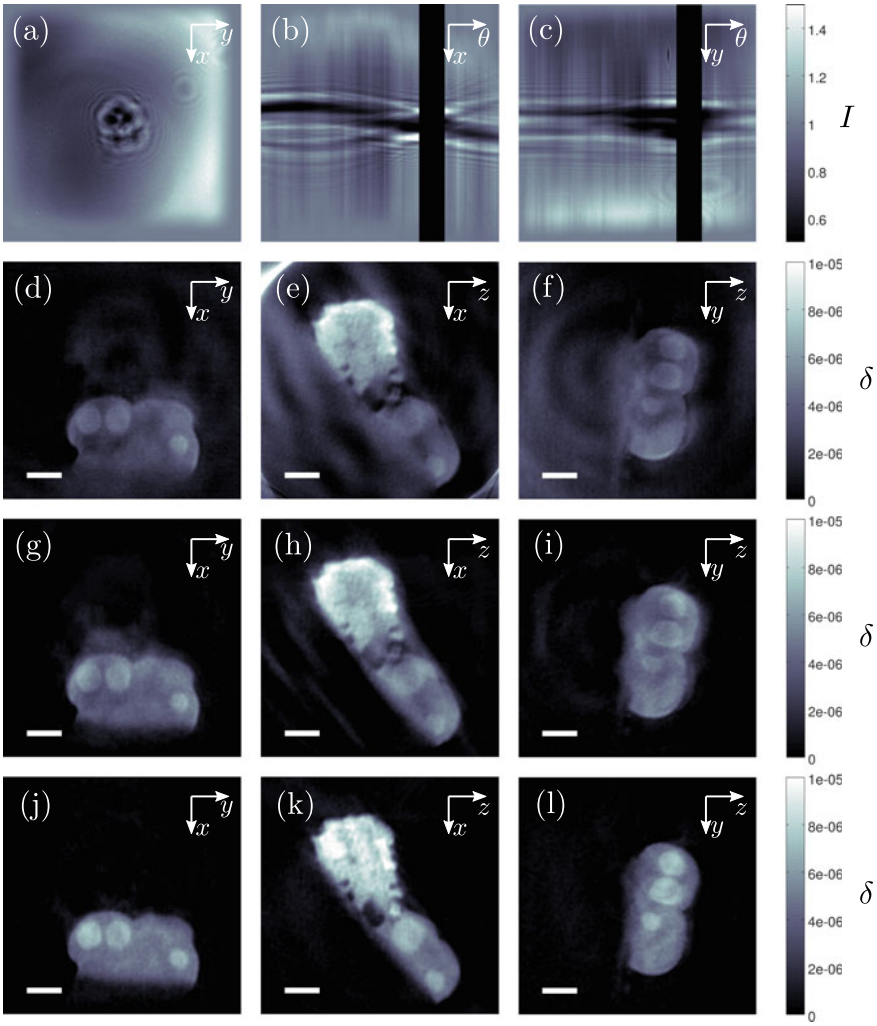

Fig. 14.4 XPCT-reconstruction of *Deinococcus radiodurans* bacteria with different algorithms. Rows show 2D orthoslices for: **a**–**c** the stack of 641 holograms of 2048 × 2048 pixels each (x, y: detector-coordinates, θ: tomographic incident angle) **d**–**l** reconstructed object-volumes with different methods (**d**–**f** CTF-inversion followed by FBP-reconstruction, **g**–**i** Linear Kaczmarz, **j**–**l** Newton-Kaczmarz). The tomographic axis is the y-axis. Scale bars: 1 μm. For details, see text

References

1. Davidoiu, V., Sixou, B., Langer, M., Peyrin, F.: Nonlinear approaches for the single-distance phase retrieval problem involving regularizations with sparsity constraints. Appl. Opt. **52**(17), 3977–3986 (2013)
2. Maretzke, S.: Regularized Newton methods for simultaneous Radon inversion and phase retrieval in phase contrast tomography (2015). arXiv preprint arXiv:1502.05073
3. Cloetens, P., Ludwig, W., Baruchel, J., Van Dyck, D., Van Landuyt, J., Guigay, J., Schlenker, M.: Holotomography: Quantitative phase tomography with micrometer resolution using hard synchrotron radiation X-rays. Appl. Phys. Lett. **75**(19), 2912–2914 (1999)
4. Hofmann, R., Moosmann, J., Baumbach, T.: Criticality in single-distance phase retrieval. Opt. Express **19**(27), 25881–25890 (2011)
5. Krenkel, M., Toepperwien, M., Alves, F., Salditt, T.: Three-dimensional single-cell imaging with X-ray waveguides in the holographic regime. Acta Crystallogr. A **73**(4), 282–292 (2017)
6. Langer, M., Cloetens, P., Guigay, J.P., Peyrin, F.: Quantitative comparison of direct phase retrieval algorithms in in-line phase tomography. Med. Phys. **35**(10), 4556–4566 (2008)
7. Turner, L., Dhal, B., Hayes, J., Mancuso, A., Nugent, K., Paterson, D., Scholten, R., Tran, C., Peele, A.: X-ray phase imaging: Demonstration of extended conditions for homogeneous objects. Opt. Express **12**(13), 2960–2965 (2004)
8. Nugent, K.A.: X-ray noninterferometric phase imaging: a unified picture. J. Opt. Soc. Am. A **24**(2), 536–547 (2007)
9. Jonas, P., Louis, A.: Phase contrast tomography using holographic measurements. Inverse Probl. **20**(1), 75 (2004)
10. Walther, A.: The question of phase retrieval in optics. J. Mod. Opt. **10**(1), 41–49 (1963)
11. Akutowicz, E.J.: On the determination of the phase of a Fourier integral, i. Proc. Am. Math. Soc., 179–192 (1956)
12. Akutowicz, E.J.: On the determination of the phase of a Fourier integral, ii. Proc. Am. Math. Soc. **8**(2), 234–238 (1957)
13. Fienup, J.: Phase retrieval algorithms: a personal tour. Appl. Opt. **52**(1), 45–56 (2013)
14. Klibanov, M.V., Sacks, P.E., Tikhonravov, A.V.: The phase retrieval problem. Inverse Probl. **11**(1), 1 (1995)
15. Luke, D.R.: Phase retrieval, what's new. SIAG/OPT Views News **25**(1), 1–5 (2017)
16. Millane, R.: Phase retrieval in crystallography and optics. J. Opt. Soc. Am. A **7**(3), 394–411 (1990)
17. Shechtman, Y., Eldar, Y.C., Cohen, O., Chapman, H.N., Miao, J., Segev, M.: Phase retrieval with application to optical imaging: a contemporary overview. IEEE Signal Proc. Mag. **32**(3), 87–109 (2015)
18. Beinert, R.: One-dimensional phase retrieval with additional interference intensity measurements. Results Math. **72**(1–2), 1–24 (2017)
19. Bendory, T., Beinert, R., Eldar, Y.C.: Fourier phase retrieval: Uniqueness and algorithms. In: Compressed Sensing and its Applications, pp. 55–91. Springer (2017)
20. Leshem, B., Xu, R., Dallal, Y., Miao, J., Nadler, B., Oron, D., Dudovich, N., Raz, O.: Direct single-shot phase retrieval from the diffraction pattern of separated objects. Nat. Commun. **7**, 10,820 (2016)
21. Raz, O., Leshem, B., Miao, J., Nadler, B., Oron, D., Dudovich, N.: Direct phase retrieval in double blind Fourier holography. Opt. Express **22**(21), 24935–24950 (2014)
22. Maretzke, S.: A uniqueness result for propagation-based phase contrast imaging from a single measurement. Inverse Probl. **31**, 065,003 (2015)
23. Gabor, D., et al.: A new microscopic principle. Nature **161**(4098), 777–778 (1948)
24. Maretzke, S., Hohage, T.: Stability estimates for linearized near-field phase retrieval in X-ray phase contrast imaging. SIAM J. Appl. Math. **77**, 384–408 (2017)
25. Kalbfleisch, S., Neubauer, H., Krüger, S., Bartels, M., Osterhoff, M., Mai, D., Giewekemeyer, K., Hartmann, B., Sprung, M., Salditt, T.: The göttingen holography endstation of beamline p10 at petra iii/desy. In: AIP Conference Proceedings, Vol. 1365, pp. 96–99. AIP (2011)

26. Salditt, T., Osterhoff, M., Krenkel, M., Wilke, R.N., Priebe, M., Bartels, M., Kalbfleisch, S., Sprung, M.: Compound focusing mirror and x-ray waveguide optics for coherent imaging and nano-diffraction. J. Synchrotron Rad. **22**(4), 867–878 (2015)
27. Havin, V., Jöricke, B.: The Uncertainty Principle in Harmonic Analysis. Springer, Berlin (1994)
28. Slepian, D., Sonnenblick, E.: Eigenvalues associated with prolate spheroidal wave functions of zero order. Bell Syst. Tech. J. **44**(8), 1745–1759 (1965)
29. Maretzke, S.: Inverse problems in propagation-based X-ray phase contrast imaging and tomography: stability analysis and reconstruction methods. eDiss Uni Göttingen (2019)
30. Kostenko, A., Batenburg, K.J., King, A., Offerman, S.E., van Vliet, L.J.: Total variation minimization approach in in-line X-ray phase-contrast tomography. Opt. Express **21**(10), 12185–12196 (2013)
31. Ruhlandt, A., Salditt, T.: Three-dimensional propagation in near-field tomographic X-ray phase retrieval. Acta Crystallogr. A **72**(2) (2016)
32. Maretzke, S.: Locality estimates for Fresnel-wave-propagation and stability of near-field X-ray propagation imaging with finite detectors. Inverse Probl. **34**(12), 124,004 (2018). https://doi.org/10.1088/1361-6420/aae78f
33. Maretzke, S., Bartels, M., Krenkel, M., Salditt, T., Hohage, T.: Regularized Newton methods for X-ray phase contrast and general imaging problems. Opt. Express **24**(6), 6490–6506 (2016)
34. Ruhlandt, A., Krenkel, M., Bartels, M., Salditt, T.: Three-dimensional phase retrieval in propagation-based phase-contrast imaging. Phys. Rev. A **89**(3), 033,847 (2014)
35. Burger, M., Kaltenbacher, B.: Regularizing Newton-Kaczmarz methods for nonlinear ill-posed problems. SIAM J. Numer. Anal. **44**(1), 153–182 (2006)
36. Guan, H., Gordon, R.: A projection access order for speedy convergence of ART (algebraic reconstruction technique): a multilevel scheme for computed tomography. Phys. Med. Biol. **39**(11), 2005 (1994)
37. Andersen, A.H., Kak, A.C.: Simultaneous algebraic reconstruction technique (SART): a superior implementation of the ART algorithm. Ultrason. Imaging **6**(1), 81–94 (1984)
38. Maretzke, S.: Generalized SART-methods for tomographic imaging. arXiv preprint p. arXiv:1803.04726 (2018)